

Competing correlated states around the zero-field Wigner crystallization transition of electrons in two dimensions

J. Falson^{1,2,3}, I. Sodemann^{4,5}, B. Skinner⁶, D. Tabrea¹, Y. Kozuka^{7,8}, A. Tsukazaki^{1,9}, M. Kawasaki^{1,1}, K. von Klitzing¹ and J. H. Smet¹

The competition between kinetic energy and Coulomb interactions in electronic systems leads to complex many-body ground states with competing orders. Here we present zinc oxide-based two-dimensional electron systems as a high-mobility system to study the low-temperature phases of strongly interacting electrons. An analysis of the electronic transport provides evidence for competing correlated metallic and insulating states with varying degrees of spin polarization. Some features bear quantitative resemblance to quantum Monte Carlo simulation results, including the transition point from the paramagnetic Fermi liquid to Wigner crystal and the absence of a Stoner transition. At very low temperatures, we resolve a non-monotonic spin polarizability of electrons across the phase transition, pointing towards a low spin phase of electrons, and a two-order-of-magnitude positive magnetoresistance that is challenging to understand within traditional metallic transport paradigms. This work establishes zinc oxide as a platform for studying strongly correlated electrons in two dimensions.

ilute interacting electrons harbour competing ground states when their Coulomb repulsion greatly exceeds their kinetic energy. In a parabolically dispersing two-dimensional electron system (2DES), the ratio of interaction to kinetic energy scales is parameterized by the dimensionless parameter r_s , given by

$$r_{\rm s} = \frac{1}{(\pi n)^{1/2} a_{\rm B}}. (1)$$

Here, $a_{\rm B}=4\pi\epsilon\hbar^2/m_{\rm b}e^2$ is the effective Bohr radius of carriers with ϵ the material dielectric constant, \hbar is the reduced Planck constant, $m_{\rm b}$ is the band effective mass, e is the elementary charge and n is the electron concentration. As the density is lowered, the electron system undergoes a Wigner crystallization transition, which quantum Monte Carlo (QMC) studies predict to occur at around $r_{\rm s}\approx 30$ (refs. ¹⁻⁷). In spite of decades of research efforts⁸⁻¹², many aspects of the phase diagram of a strongly interacting 2DES in the limit of zero temperature and zero magnetic field remain clouded in the range of $25 < r_{\rm s} < 40$. One of the main obstacles has been the trade-off of interaction and disorder strengths in these platforms; the cleanest systems, such as electron-doped GaAs, are also typically the ones that are relatively weakly interacting, while those with stronger interactions tend to be more disordered. Thus, systematic experimental studies in the high $r_{\rm s}$ regime ($r_{\rm s} \ge 20$) remain few ¹³⁻¹⁴.

ZnO heterostructures offer a platform that is sufficiently strongly interacting and clean $^{15,16}.$ Here, the 2DES is formed due to the polarization mismatch between epitaxial layers of Mg-alloyed Mg_xZn_1-xO and pristine ZnO, both of which exist in the inversion

asymmetric wurtzite crystal structure ($P6_3mc$ space group). The itinerant carriers occupy a potential well in ZnO in a predominantly Zn²⁺s-orbital-like single electron pocket at Γ with weak non-parabolicity and spin–orbit interaction¹⁷. The band is highly spin degenerate, and the band g-factor (g_b) (~2) is isotropic¹⁸. The enhanced electronic interactions stem from the ionicity of the crystal, which produces a relatively heavy band mass (m_b =0.3 m_0) and small dielectric constant (ϵ =8.5 ϵ_0), where m_0 is the bare electron mass and ϵ_0 is the vacuum permittivity. These features combine to make the system close to the ideal jellium model studied in QMC. The interaction effects and cleanness of the system are evidenced by the observation of fragile correlated states in the fractional quantum Hall regime, such as the 3/2, 5/2 and 7/2 incompressible states, bubbles and stripes^{19,20}, with the devices remaining strongly interacting at zero magnetic field, as we demonstrate in this study.

Transport properties of the device

The quasi-Hall bar device under study is rendered in Fig. 1a. The MgZnO/ZnO heterostructure confines a 2DES approximately 500 nm beneath the wafer surface with n tuned in situ via a capacitively coupled gate electrode on the back side of the wafer. The field-effect transfer characteristics are displayed in Fig. 1b. Here, n is determined from the period of quantum oscillations and Hall effect. Great effort has been invested to perform experiments at very low temperatures. To this end, the sample is immersed within a liquid 3 He bath in a cryostat that operates down to temperature $T \approx 7$ mK. The electrical characteristics are probed in a four-point configuration by sweeping the d.c. bias (V_{bias}) while measuring the current

¹Max-Planck-Institute for Solid State Research, Stuttgart, Germany. ²Department of Applied Physics and Materials Science, California Institute of Technology, Pasadena, CA, USA. ³Institute for Quantum Information and Matter, California Institute of Technology, Pasadena, CA, USA. ⁴Institut für Theoretische Physik, Universität Leipzig, Leipzig, Germany. ⁵Max-Planck-Institute for the Physics of Complex Systems, Dresden, Germany. ⁶Department of Physics, Ohio State University, Columbus, OH, USA. ⁷Research Center for Magnetic and Spintronic Materials, National Institute for Materials Science, Tsukuba, Japan. ⁸PRESTO, JST, Kawaguchi, Japan. ⁹Institute for Materials Research, Tohoku University, Sendai, Japan. ¹⁰Department of Applied Physics and Quantum-Phase Electronics Center (QPEC), University of Tokyo, Tokyo, Japan. ¹¹RIKEN Center for Emergent Matter Science (CEMS), Wako, Japan. ¹²e-mail: falson@caltech.edu

ARTICLES NATURE MATERIALS

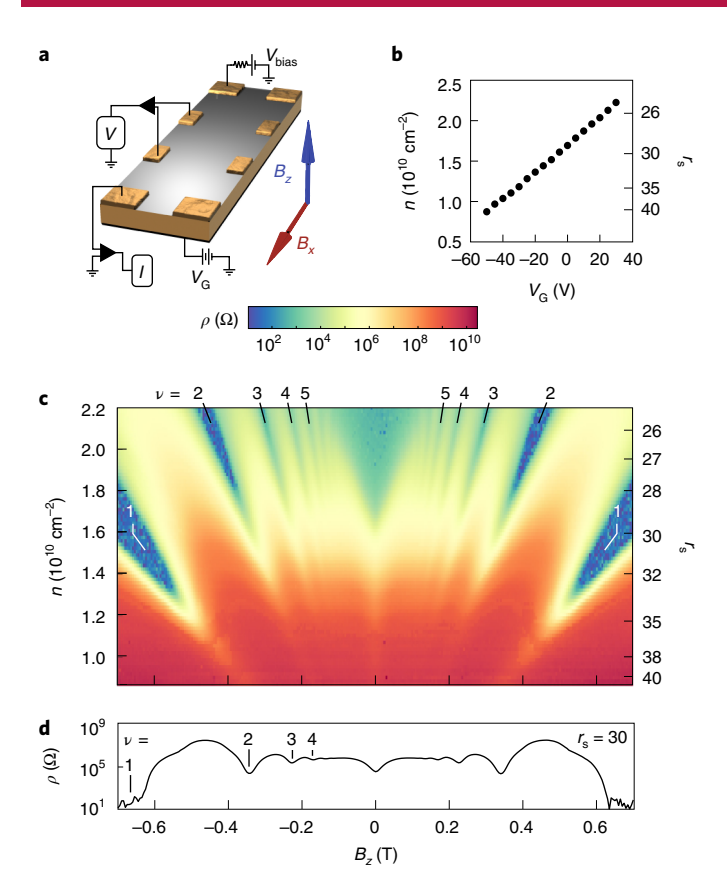


Fig. 1 | The device and quantum transport. a, Schematic of the device under study. **b**, Charge carrier density (n) as a function of gate bias ($V_{\rm G}$). **c**, Mapping of ρ as a function of B_z and n, taken in the limit $I \rightarrow 0$ nA where $T \approx 10$ mK. Integer quantum Hall filling factors ν are noted. **d**, Line trace of magnetoresistance corresponding to $n = 1.6 \times 10^{10}$ cm⁻² and $r_s = 30$.

across the device (I) and local longitudinal voltage drop (V), yielding a single I-V trace. The first derivative of this data provides the differential resistance (dV/dI) of the device as a function of I. We define ρ to be dV/dI in the small current limit ($I \rightarrow 0$ nA), which probes the linear response of the equilibrium state of the system.

The magnetotransport of the device in the (B_z,n) parameter space where B_z is the out-of-plane magnetic field is presented in Fig. 1c. Oscillatory features in ρ as $|B_z|$ is increased are associated with integer steps in Landau quantization. These states are labelled according to their filling factor $\nu=hn/eB_z$, where h is the Planck constant. A magnetotransport trace at $n=1.6\times 10^{10}\,\mathrm{cm^{-2}}$ ($r_s=30$) is displayed in Fig. 1d with a robust $\nu=1$ quantum Hall state evident. Remarkably, this minimum remains apparent even when the zero-field resistance increases to approximately $10^8\Omega$ as the density is reduced to $n=1.3\times 10^{10}\,\mathrm{cm^{-2}}$ ($B_z=0.5\,\mathrm{T}$).

The data in Fig. 2a present $\rho(n,T)$ of the device at zero magnetic field. This data reveal a crossover from a metallic $\mathrm{d}\rho/\mathrm{d}T>0$ to insulating dependence $\mathrm{d}\rho/\mathrm{d}T<0$ at a critical density $n_c\approx 1.6\times 10^{10}\,\mathrm{cm}^{-2}$ (corresponding to $r_s=30$), enabling us to associate the density n_c with a zero-field metal–insulator transition (MIT) close to the quantum resistance value h/e^2 . Data for $T\lesssim 20\,\mathrm{mK}$ deviate from the systematic behaviour at higher temperatures, most likely due to the common issue of decoupling of the electron temperature from that of the immersion cryogen. The effect of an in-plane magnetic field is displayed in Fig. 2b, which indicates a positive magnetoresistance at all values of n. The value $\rho=h/e^2$ is identified as a black line, which corresponds to a finite B_x where B_x is the magnetic field projected in-plane when n is larger than n_c .

Examining spin susceptibility. The in-plane magnetic field permits us to control the degree of spin polarization of the electrons, as the orbital coupling to in-plane fields is negligible due to the two-dimensional confinement. Figure 3a plots the magnetoresistance of the device as a function of B_r at $n = 2 \times 10^{10}$ cm⁻² and at various temperatures. From these curves we can identify two values of the magnetic field of interest: B_c , which is interpreted as the critical magnetic field required to reach full spin polarization, and is identified as the point at which ρ saturates to a value of $\rho_{R=sat}$ (black triangle) and can be interpreted as the critical field required to reach full spin polarization^{8–12}, and B^* , at which there is a change in the sign of $d\rho/dT$ from metallic-like to insulating-like. The large dynamic range of ρ of the device makes it challenging to identify $B_c(n)$ in Fig. 2b, and thus we plot the ratio ρ_B/ρ_{B-sat} where ρ_B is the resistivity at a given magnetic field in the (B_x, n) plane in Fig. 3b. This aids visual identification of B_c as the fully spin-polarized 2DES appears as an orange colour for any n in the figure. The data in Fig. 3b reveal a non-monotonic dependence of B_c as a function of n (dashed line) as the MIT is crossed. We observe an inflection point in the value of B_c/n around $n = 1.8 \times 10^{10}$ cm⁻² (Fig. 3d), which is higher than the value n_c associated with the zero-field MIT. While the procedure for determining B_c can be performed in multiple ways, as is discussed in Supplementary Section 10, a qualitatively similar trend is obtained. The in-plane field traces also reveal the presence of finite magnetoresistance even in the low-density limit (Fig. 3c), where the device is insulating for all magnetic fields.

The dotted line in Fig. 3b tracks B^* , and thus, the (B_s,n) parameter space hosts two regions with an insulating-like temperature dependence $\mathrm{d}\rho/\mathrm{d}T<0$, namely at $B>B^*$ when $n>n_c$, and at all B_s when $n< n_c$. As we show in Supplementary Section 7, in the latter regime of $n< n_c$, the temperature dependence is consistent with the activated or variable range hopping mechanisms that are characteristic of insulators²¹ (including Wigner crystals²²). By contrast, in the regime of $n>n_c$ and $B>B^*$ where we encounter what appears as a field-induced MIT, the dependence of resistivity on temperature is more consistent with a linear or power-law relation. Such a linear increase in ρ with T, and the accompanying change in sign of $\mathrm{d}\rho/\mathrm{d}T$, has been shown theoretically to arise in metallic, correlated states with high spin polarization^{23,24}. Thus, the temperature dependence points to a ground state at $n>n_c$ and $B>B_c$ that is distinct from the low-density insulating phase for $n<n_c$ at $r_s>30$.

The value of B_c allows us to measure the renormalized spin susceptibility of the system, χ . Experimentally, it is convenient to use the following relationship:

$$\frac{B_{\rm c}}{n} \approx \frac{2\pi\hbar^2}{\mu_{\rm B}} \frac{1}{g^*m^*}.$$
 (2)

Here, $\mu_{\rm B}$ is the Bohr magneton. The quasiparticle effective mass (m^*) and effective g-factor (g^*) are related to the renormalized susceptibility $g^*m^*/m_0 = 4\pi g_0 \chi$ (Supplementary Section 4), where g_0 is the bare electron g-factor. The B_c/n is presented in Fig. 3d as a function of n with corresponding values of g^*m^*/m_0 plotted as vertical lines. As is observed from much higher densities (Supplementary Fig. 5), g^*m^*/m_0 increases monotonically with decreasing n in the range $2.3 > n > 1.8 \times 10^{10}$ cm⁻². The estimated value of $g^*m^*/m_0 \approx 15$ at $n = n_c$ represents a nearly 30-fold enhancement over the band value of 0.6. The relative magnitude of the magnetoresistance with in-plane field, $\rho_{\rm B=0}/\rho_{\rm B=sat}$, is generally suppressed when reducing n (Fig. 3e). However, the non-trivial dependence of the magnetoresistance never disappears completely, as we discuss below.

Nonlinear charge transport is encountered throughout the parameter space and is revealed by studying the differential resistance as a function of current. Figure 4a-c plots I-V traces at three distinct charge densities, corresponding to $r_s \approx 25$, 28 and

NATURE MATERIALS ARTICLES

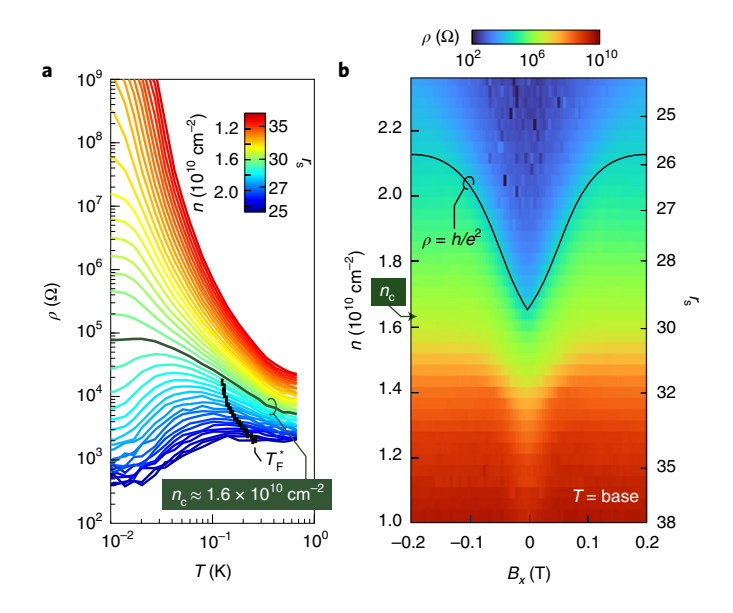


Fig. 2 | The metal-insulator transition. **a**, Temperature dependence of ρ as n is tuned. The trace associated with $n_c \approx 1.6 \times 10^{10}$ cm⁻² is plotted as a bold line. T_F is the effective Fermi temperature at a given n. **b**, The ρ in the (B_n, n) plane for the device. The condition for $\rho = h/e^2$ is indicated by the black line.

32, respectively (purple, blue and red triangles). The corresponding differential resistance as a function of *I* is plotted in Fig. 4d–f. The three values of r_s represent qualitatively distinct responses in the (n, T, V) parameter space. For $r_c \approx 25$ the system displays metallic $(d\rho/dT > 0)$ transport as the lowest attainable temperature is approached, with dV/dI approximately constant as a function of I. By contrast, strong nonlinearity develops as $T \to 0$ when $n < n_c$. We characterize this nonlinearity in two different ways: through the threshold voltage (V_T) at which 10 pA flows through the device, and through an extrapolation of the high current voltage drop to zero current (ΔV), as shown in Fig. 4c. A large V_T is a characteristic transport feature expected from a Wigner crystal (WC) ground state^{13,25}, arising from pinning of the crystal. We also identify a regime of apparent excess conductance at low bias for a finite range of densities, $n_c < n < 2 \times 10^{10} \,\mathrm{cm}^{-2}$ (Fig. 4b,e). In this regime, a flattening of the voltage drop as a function of current is visually apparent in the raw I-V data (Fig. 4b), producing a lower differential resistance dV/dI as $I \rightarrow 0$. The differential resistance increases by as much as four times when even a few nanoamperes of current (corresponding to ~1 fW power dissipation) are fed through the device. This excess conductance is discussed

The degree of nonlinearity in the parameter space is not evident in the raw resistance value of Fig. 2a, yet it provides additional insight into the qualitative nature of the ground state. To illustrate this, we plot the ratio of zero-bias resistance ρ with that at finite current, here defined as the resistance at $I \approx 2.5$ nA ($\rho_{2.5\text{nA}}$). We present this in two panels: the (n,T) plane at zero field (Fig. 4g), and in the (n,B_x) plane at base temperature (Fig. 4h). In both these representations, green regions (where $\rho/\rho_{2.5\text{nA}}$ is close to unity) correspond to a linear response where the differential resistance is independent of *I*, as is evident for all n when $T \ge 100 \,\mathrm{mK}$. Some region of excess conductivity, defined as $\rho < \rho_{2.5\text{nA}}$, appears as a dome-like blue region above n_c , disappears above 30 mK and is suppressed with the application of a B field (Supplementary Fig. 12). Similar I-V features have been identified in previous studies as the MIT is approached^{13,26}. Both yellow and red regions corresponds to a peak in ρ at I=0 nA, with the former displaying weaker nonlinearity in the form of a finite ΔV and the latter hosting a prominent V_T as $I \rightarrow 0$.

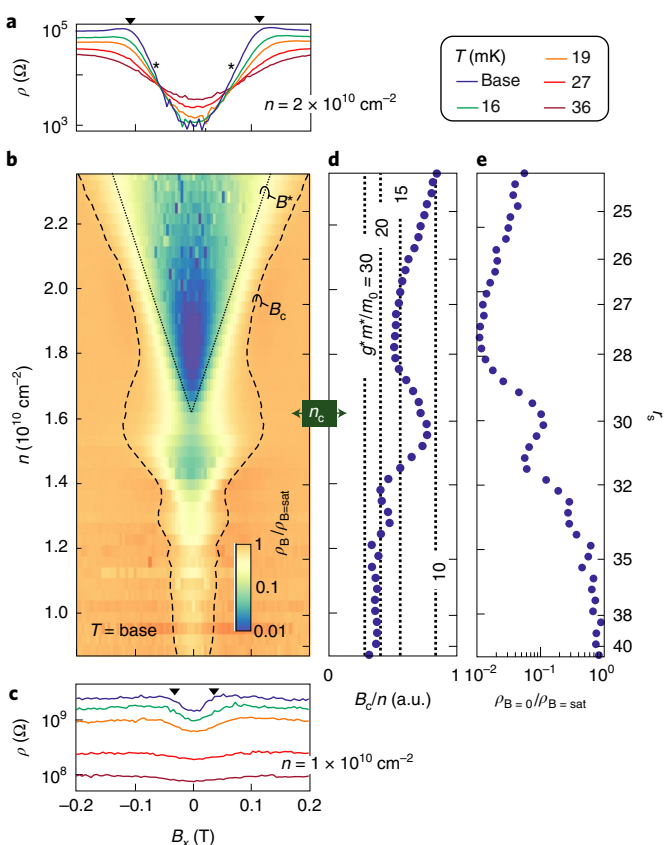


Fig. 3 | Spin polarization in an in-plane magnetic field. **a**, Temperature dependence of ρ as a function of B_x at $n=2\times10^{10}$ cm⁻² with B_c indicated by inverted triangles and B^{**} by stars. **b**, Mapping of the normalized differential resistance $\rho_B/\rho_{B=sat}$ as a function of B_x and n. The values of B_c and B^* are indicated by dashed and dotted lines, respectively. Here, $T\approx10$ mK. **c**, Temperature dependence of ρ as a function of B_x at $n=1\times10^{10}$ cm⁻². **d**, The B_c/n as a function of n at base temperature. Corresponding values of g^*m^*/m_0 are indicated as vertical dotted lines. **e**, Magnitude of magnetoresistance $\rho_{B=0}/\rho_{B=sat}$ as a function of n.

Discussion. We characterize the phases encountered using the boundaries associated with full spin polarization of the system (B_c , dashed line), the change in sign of $d\rho/dT$ (B^* , dotted line), the magnitude of the resistivity relative to h/e^2 (black line) and the degree of nonlinearity $\rho/\rho_{2.5nA}$, all of which are plotted in Fig. 4h. We couple these experimental results with a comparison to state-of-the-art QMC simulations⁷, which have identified a competition between paramagnetic Fermi liquid (FL), spin-polarized FL, antiferromagnetic WC with a stripe-like spin order on a triangular lattice and spin-polarized WC phases in the r_s range studied in our work. Here we expand the phase diagram produced by QMC to take into account a finite in-plane magnetic field (Supplementary Information for details and alternative scenarios). The result is presented in Fig. 4i and contains no free parameters.

We associate the zero-field metal phase at large n with a paramagnetic FL subjected to increasingly strong interactions as n is reduced towards n_c . At finite B_x and $n > n_c$, however, the change in sign of $\mathrm{d}\rho/\mathrm{d}T$ at B^* that is traditionally associated with a MIT bears closer resemblance to a linear-in-T correction to the conductivity emerging from strong interactions in a FL^{23,24}. We also note that the magnetic field scale at which the paramagnetic FL is predicted by QMC calculations to become the spin-polarized FL (Fig. 4i) agrees with the measured value of B^* (or B_c) without any fitting parameters. Therefore we associate the state that appears for $n > n_c$

ARTICLES NATURE MATERIALS

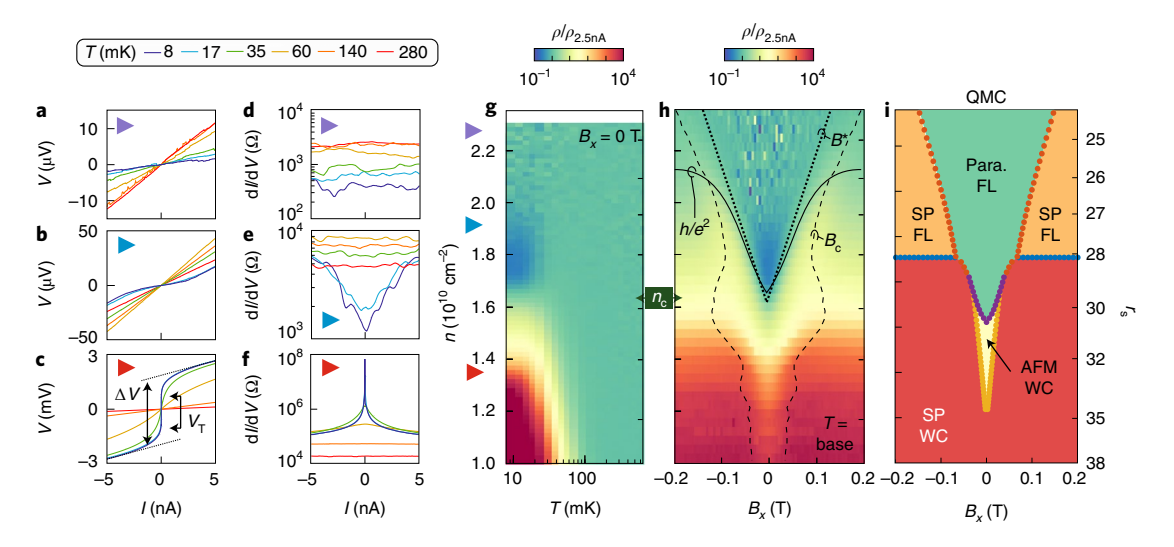


Fig. 4 | Nonlinear transport characteristics and phase diagram. a-c, Temperature dependent I-V sweeps when $r_s \approx 25$ (**a**), 28 (**b**) and 32 (**c**) and $B_x = 0$ T. Note the schematic representation of V_T and ΔV in **c**. **d-f**, The dV/dI of the datasets in **a-c**. Coloured triangles highlight the three regimes discussed in the text. **g,h**, Degree of nonlinearity plotted as $\rho/\rho_{2.5nA}$ as a function of n and T at B = 0 (**g**), and as a function of n and B_x at base temperature (**h**). The dashed, dotted and solid lines represent B_c , B^* and $\rho = h/e^2$ conditions. **i**, QMC ground states with the addition of a finite B field. Para., paramagnetic; AFM, antiferromagnetic; SP, spin-polarized.

and $B > B_c$ as the spin-polarized FL. However, while such a linear increase in ρ is consistent with our data (Supplementary Section 7), we caution that the theory of some studies in the literature^{23,24} is not a priori applicable to the states with relatively large r_s and large resistivity that we are considering. In line with this concern, it is worth emphasizing that our results in this regime exhibit extreme deviations from the usual weak-coupling metallic conductivity, as evidenced, for example, by the 100-fold positive magnetoresistance and by a low-temperature resistance substantially higher than h/e^2 .

Turning our attention to $n < n_c$, the insulating phase has the characteristic transport attributes of a pinned WC, as evidenced by the large value of V_T that develops at low temperature. The vanishing of the nonlinearity at temperatures above approximately $T = 50 \,\mathrm{mK}$ is consistent with thermal melting of a WC²⁷. The nonlinearity in this regime is orders of magnitude larger than that of the spin-polarized FL phase discussed above, supporting our hypothesis that the two regimes host distinct phases. The positive magnetoresistance at $n < n_c$ that becomes clear at very low temperatures in Fig. 3c remains to be fully understood, although it is apparently consistent with calculations²⁸ that consider the effect of Zeeman splitting of localized states on hopping conduction. The presence of finite magnetoresistance appears to preclude the conclusion that the state is fully spin polarized at low temperature in the range of r_s studied. This is in contrast with a recent study of aluminium arsenides¹⁴, which reported an apparent divergence of the spin susceptibility in the insulating phase based upon no appreciable magnetoresistance for $n < n_c$ at a measurement temperature of $T \approx 300 \,\mathrm{mK}$ (Supplementary Section 6 for a discussion). The lack of clear spontaneous spin polarization at very low temperatures in our experiment agrees with the fact that the exchange energy scale J associated with spin ferromagnetic ordering of the WC at $n < n_c$, as estimated by QMC, is smaller than |J| < 10 mK (Supplementary Section 6). The spins of the WC are therefore likely disordered by temperature fluctuations at $B_r = 0$. While we note that delicate hysteretic features in transport are indeed resolved for $n \le n_c$, which upon first glance could indicate some ferromagnetic ordering (Supplementary Fig. 7), we, however, ascribe these features to experimental artefacts associated with heating close to zero field and trapped flux in the superconducting coil, as the estimated coercive field in the presence of magnetostatic fields is ~10⁻⁷T (Supplementary Section 5) and hence undetectable in experiment.

We now discuss one of the most remarkable findings of our study, namely the non-monotonicity of the in-plane saturation field B_c near the zero-field MIT. The non-monotonicity of B_c is a low-temperature property of the system and is absent above approximately 30 mK (Supplementary Fig. 4). In agreement with QMC calculations7, we find no clear evidence for a Stoner instability of the itinerant liquid; finite magnetoresistance is always present in the metal phase. By contrast, QMC has identified a possible antiferromagnetic crystal in between the paramagnetic FL and the fully spin-polarized WC. By adapting the QMC results from a study in the literature to include the in-plane field (Supplementary Section 3 for details), one obtains the phase diagram shown in Fig. 4i. However, as we see from this phase diagram, the intermediate antiferromagnetic state does not offer any clear explanation for the non-monotonicity of the critical field B_c to spin polarize the system. Moreover, as mentioned before, our lowest temperature scale $T \approx 20 \,\mathrm{mK}$ is larger than the exchange energy scale J, or more precisely it is larger than the energy difference per electron of the ferromagnetic WC and the antiferromagnetic WC obtained from QMC, as detailed in Supplementary Section 6, and thus the spin order of the WC is likely destroyed by temperature fluctuations at $B_r = 0$. We therefore believe that the antiferromagnetic WC phase found in QMC is not likely to be the origin of the non-monotonicity of B_c that we observe. We note that the QMC employed in the literature is variational in nature, and therefore it is always possible that other phases not considered could be behind the non-monotonicity of B_c , such as spin liquid states^{29,30} or spin-density-wave ordered states^{31,32}.

The role of spatial variation in electron density may also be prominent in the vicinity of $n=n_c$. Even in the cleanest samples it is not possible to completely eliminate the role of disorder, which tends to produce variation in the local electron density, and leaves the WC phase with only finite-range order. When the average density is very close to n_c , such variation causes the 2DES to break up into itinerant and localized regions (Supplementary Section 8 for a discussion). And even in the absence of disorder, variation in the local density can arise from Coulomb-frustrated phase separation $^{6,33-35}$. While such phase separation may be important near $n=n_c$, it does not provide an obvious explanation for the non-monotonicity of B_c as a function of n. Nevertheless, the phase separation picture can serve as a premise for interpreting the excess conductance presented

NATURE MATERIALS ARTICLES

in Fig. 4b,e. When conducting and insulating phases are mixed in nearly equal proportion, then electric current flows predominantly through narrow metallic pathways, which are unusually sensitive to Joule heating. The ratio of metallic to insulating regions falls as the MIT is approached, with the MIT signifying the transition to a regime where insulating regions percolate and metallic regions are relegated to disconnected puddles (Supplementary Section 9).

Finally, we note that while the QMC data used to produce Fig. 4i assume a pure 1/r Coulomb interaction at all values of the electron-electron separation r, in reality the finite thickness of the quantum well truncates the small-r divergence of the Coulomb potential. The magnitude of such an effect depends on the ratio between the effective thickness $t_{\rm WF}$ of the electron wave function and the inter-electron spacing, or in other words on the parameter $k_{\rm F}t_{\rm WF}$ where $k_{\rm F}$ is the Fermi wavenumber. We estimate that near $n=n_{\odot}$, the value of $k_{\rm F}t_{\rm WF}$ is on the order of 0.3. The smallness of this parameter justifies the comparison to the existing QMC studies, although the degree to which the phase diagram presented in Fig. 4i is altered quantitatively by such values of $k_{\rm F}t_{\rm WF}$ remains to be studied in detail theoretically.

Outlook

Our study provides experimental clarity about the phase diagram around the Wigner crystallization transition at $r_s \approx 30$ and very low temperatures. The data reveal a paramagnetic FL that exhibits a strong renormalization of its spin susceptibility, becoming nearly 30 times larger than the band value as the critical density n_c is approached. At $n < n_c$ the transport becomes strongly nonlinear and exhibits an exponential temperature dependence, both of which features are consistent with a WC. The qualitative and quantitative agreement of our phase diagram with state-of-the-art QMC⁷ is striking, with zero adjustable parameters. Future experimental work will probe the finite-range order within the pinned solid phase, for example through optical absorption^{36,37}, reflection^{38,39} or tunnelling approaches⁴⁰. The most prominent mystery suggested by our measurements is the possible existence and nature of a WC state with incomplete spin polarization. The non-monotonicity of the magnetic field B_c required to achieve spin polarization has no obvious interpretation in terms of the QMC phase diagram and may be associated either with the spatial coexistence of different phases or with an as-yet-undetermined intermediate phase. The large increase of resistance with the in-plane field, which for densities near n_c becomes as large as two orders of magnitude, is also incompletely understood. QMC calculations suggest that the state at $B > B_c$ and n slightly larger than n_c is a spin-polarized FL, but the large value of resistance poses a challenge for understanding this state within traditional paradigms of metallic transport.

Online content

Any methods, additional references, Nature Research reporting summaries, source data, extended data, supplementary information, acknowledgements, peer review information; details of author contributions and competing interests; and statements of data and code availability are available at https://doi.org/10.1038/s41563-021-01166-1.

Received: 14 April 2021; Accepted: 4 November 2021; Published online: 23 December 2021

References

- Tanatar, B. & Ceperley, D. M. Ground state of the two-dimensional electron gas. *Phys. Rev. B* 39, 5005–5016 (1989).
- Rapisarda, F. & Senatore, G. Diffusion Monte Carlo study of electrons in two-dimensional layers. *Aust. J. Phys.* 49, 161–182 (1996).
- Phillips, P., Wan, Y., Martin, I., Knysh, S. & Dalidovich, D. Superconductivity in a two-dimensional electron gas. *Nature* 395, 253–257 (1998).

 Chamon, C., Mucciolo, E. R. & Castro Neto, A. H. P-wave pairing and ferromagnetism in the metal-insulator transition in two dimensions. *Phys. Rev. B* 64, 245115 (2001).

- Attaccalite, C., Moroni, S., Gori-Giorgi, P. & Bachelet, G. B. Correlation energy and spin polarization in the 2D electron gas. *Phys. Rev. Lett.* 88, 256601 (2002).
- Spivak, B. & Kivelson, S. A. Phases intermediate between a two-dimensional electron liquid and Wigner crystal. *Phys. Rev. B* 70, 155114 (2004).
- Drummond, N. D. & Needs, R. J. Phase diagram of the low-density twodimensional homogeneous electron gas. *Phys. Rev. Lett.* 102, 126402 (2009).
- Spivak, B., Kravchenko, S. V., Kivelson, S. A. & Gao, X. P. A. Colloquium: transport in strongly correlated two dimensional electron fluids. *Rev. Mod. Phys.* 82, 1743–1766 (2010).
- Abrahams, E., Kravchenko, S. V. & Sarachik, M. P. Metallic behavior and related phenomena in two dimensions. Rev. Mod. Phys. 73, 251–266 (2001).
- Kravchenko, S. V. & Sarachik, M. P. Metal-insulator transition in two-dimensional electron systems. Rep. Prog. Phys. 67, 1–44 (2003).
- Shashkin, A. A. & Kravchenko, S. V. Recent developments in the field of the metal-insulator transition in two dimensions. *Appl. Sci.* https://doi. org/10.3390/app9061169 (2019).
- Dolgopolov, V. T. Two-dimensional system of strongly interacting electrons in silicon (100) structures. *Phys. Usp.* 62, 633–648 (2019).
- Yoon, J., Li, C. C., Shahar, D., Tsui, D. C. & Shayegan, M. Wigner crystallization and metal-insulator transition of two-dimensional holes in GaAs at B = 0. *Phys. Rev. Lett.* 82, 1744–1747 (1999).
- Hossain, M. S. et al. Observation of spontaneous ferromagnetism in a two-dimensional electron system. *Proc. Natl Acad. Sci. USA* 117, 32244–32250 (2020).
- 15. Falson, J. et al. MgZnO/ZnO heterostructures with electron mobility exceeding $1\times10^6\,\mathrm{cm^2/Vs}$. Sci. Rep. 6, 26598 (2016).
- Falson, J. & Kawasaki, M. A review of the quantum Hall effects in MgZnO/ ZnO heterostructures. Rep. Prog. Phys. 81, 056501 (2018).
- Maryenko, D. et al. Interplay of spin-orbit coupling and Coulomb interaction in ZnO-based electron system. Nat. Commun. 12, 3180 (2021).
- Kozuka, Y. et al. Rashba spin-orbit interaction in a Mg_xZn_{1-x}O/ZnO two-dimensional electron gas studied by electrically detected electron spin resonance. *Phys. Rev. B* 87, 205411 (2013).
- Falson, J. et al. Even denominator fractional quantum Hall physics in ZnO. Nat. Phys 11, 347–351 (2015).
- Falson, J. et al. A cascade of phase transitions in an orbitally mixed half-filled Landau level. Sci. Adv. 4, eaat8742 (2018).
- Shklovskii, B. I. & Efros, A. L. Electronic Properties of Doped Semiconductors (Springer, 1984).
- Shklovskii, B. I. Coulomb gap and variable range hopping in a pinned Wigner crystal. *Phys. Status Solidi C* 1, 46–50 (2004).
- Zala, G., Narozhny, B. N. & Aleiner, I. L. Interaction corrections at intermediate temperatures: magnetoresistance in a parallel field. *Phys. Rev. B* 65, 020201 (2001).
- Zala, G., Narozhny, B. N. & Aleiner, I. L. Interaction corrections at intermediate temperatures: longitudinal conductivity and kinetic equation. *Phys. Rev. B* 64, 214204 (2001).
- Knighton, T. et al. Evidence of two-stage melting of Wigner solids. Phys. Rev. B 97, 085135 (2018).
- 26. Kravchenko, S. V., Simonian, D., Sarachik, M. P., Mason, W. & Furneaux, J. E. Electric field scaling at a *B* = 0 metal-insulator transition in two dimensions. *Phys. Rev. Lett.* 77, 4938–4941 (1996).
- Das Sarma, S. & Hwang, E. H. Low-density finite-temperature apparent insulating phase in two-dimensional semiconductor systems. *Phys. Rev. B* 68, 195315 (2003).
- Matveev, K. A., Glazman, L. I., Clarke, P., Ephron, D. & Beasley, M. R. Theory of hopping magnetoresistance induced by Zeeman splitting. *Phys. Rev. B* 52, 5289–5297 (1995).
- Chakravarty, S., Kivelson, S., Nayak, C. & Voelker, K. Wigner glass, spin liquids and the metal-insulator transition. *Phil. Mag. B* 79, 859–868 (1999).
- Bernu, B., Cândido, L. & Ceperley, D. M. Exchange frequencies in the 2D Wigner crystal. *Phys. Rev. Lett.* 86, 870–873 (2001).
- Bernu, B., Delyon, F., Holzmann, M. & Baguet, L. Hartree-Fock phase diagram of the two-dimensional electron gas. Phys. Rev. B 84, 115115 (2011).
- Bernu, B., Delyon, F., Baguet, L. & Holzmann, M. Periodic ground states of the electron gas in two and three dimensions. *Contrib. Plasma Phys.* 57, 524–531 (2017).
- Jamei, R., Kivelson, S. & Spivak, B. Universal aspects of Coulomb-frustrated phase separation. *Phys. Rev. Lett.* 94, 056805 (2005).
- Spivak, B. & Kivelson, S. A. Transport in two dimensional electronic micro-emulsions. *Ann. Phys.* 321, 2071–2115 (2006).
- Li, S., Zhang, Q., Ghaemi, P. & Sarachik, M. P. Evidence for mixed phases and percolation at the metal-insulator transition in two dimensions. *Phys. Rev. B* 99, 155302 (2019).
- Andrei, E. Y. et al. Observation of a magnetically induced Wigner solid. Phys. Rev. Lett. 60, 2765–2768 (1988).

ARTICLES NATURE MATERIALS

- Ye, P. D. et al. Correlation lengths of the Wigner-crystal order in a two-dimensional electron system at high magnetic fields. *Phys. Rev. Lett.* 89, 176802 (2002).
- 38. Smolenski, T. et al. Signatures of Wigner crystal of electrons in a monolayer semiconductor. *Nature* **595**, 53–57 (2021).
- 39. Zhou, Y. et al. Bilayer Wigner crystals in a transition metal dichalcogenide heterostructure. *Nature* **595**, 48–52 (2021).
- Jang, J., Hunt, B. M., Pfeiffer, L. N., West, K. W. & Ashoori, R. C. Sharp tunnelling resonance from the vibrations of an electronic Wigner crystal. *Nat. Phys.* 13, 340–344 (2017).

Publisher's note Springer Nature remains neutral with regard to jurisdictional claims in published maps and institutional affiliations.

© The Author(s), under exclusive licence to Springer Nature Limited 2022

NATURE MATERIALS ARTICLES

Methods

The heterostructure was grown using ozone-assisted molecular beam epitaxy and consists of a lightly alloyed Mg_xZn_{1-x}O layer ($x \approx 0.001$) of 500 nm thickness grown on a homoepitaxial ZnO layer upon single crystal (0001) Zn-polar ZnO substrates^{15,16}. The heterostructure has an estimated electron mobility of approximately 600,000 cm² V⁻¹ s⁻¹ in the metallic regime (Supplementary Information for discussion). Ohmic contacts were formed by evaporating Ti (10 nm) followed by Au (50 nm) on the sample surface. Indium was additionally soldered upon these pads to improve the contact quality. The distance between voltage probes is approximately 1 mm. The sample was immersed in a liquid 3He containing polycarbonate cell attached to the end of a cold finger of a dilution refrigerator cryostat equipped with a three-axis (9–3–1 T) vector magnet. The ³He cell is based upon previous reports^{41,42}. The mixing chamber temperature is measured using a calibrated cerous magnesium nitrate paramagnetic thermometer for $7 \le T \le 120$ mK, and a ruthenium oxide thermometer for $50 \le T \le 800$ mK. Each measurement wire passes through a large-surface-area ($A \approx 1 \text{ m}^2$) sintered silver heat exchanger to overcome the Kapitza resistance that suppresses heat exchange at low T. The differential resistance data are obtained by measuring I-V data using DL Instruments 1211 current and 1201 voltage preamplifiers at discrete steps in the (B,T,n) parameter space, followed by differentiation using data analysis software.

Data availability

The data that support the findings of this study are available from the corresponding author on request.

References

- 41. Pan, W. et al. Exact quantization of the even-denominator fractional quantum Hall state at $\nu=5/2$ Landau level filling factor. *Phys. Rev. Lett.* **83**, 3530–3533 (1999).
- 42. Samkharadze, N. et al. Integrated electronic transport and thermometry at millikelvin temperatures and in strong magnetic fields. *Rev. Sci. Instrum.* **82**, 053902 (2011).

Acknowledgements

We appreciate discussions with I. Aleiner, J. Checkelsky, S. Das Sarma, N. Drummond, J. Eisenstein, S. Kivelson, C. Murthy, B. Narozhny, B. Spivak and A. Young, along with technical support from J.-S. Xia, N. Sullivan, G. Euchner and S. Wahl. J.F. acknowledges support from the Max Planck Institute, University of British Columbia and University of Tokyo Center for Quantum Materials, the Deutsche Forschungsgemeinschaft (FA 1392/2-1); and the Institute for Quantum Information and Matter, a National Science Foundation Physics Frontiers Center (grant PHY-1733907). B.S. acknowledges support from the National Science Foundation under grant DMR-2045742. Y.K. acknowledges the Japan Science and Technology Agency, PRESTO grant number JPMJPR1763, Japan. M.K. acknowledges the financial support of the Japan Science and Technology Agency, CREST grant number JPMJCR16F1, Japan.

Author contributions

J.F. and D.T. gathered experimental data. J.F. performed the molecular beam epitaxy with assistance from Y.K., A.T. and M.K. J.F., I.S. and B.S. wrote the manuscript. All authors discussed the results and commented on the manuscript.

Competing interests

The authors declare no competing interests.

Additional information

Supplementary information The online version contains supplementary material available at https://doi.org/10.1038/s41563-021-01166-1.

Correspondence and requests for materials should be addressed to J. Falson.

Peer review information Nature Materials thanks Rui-Rui Du, Raymond Ashoori and the other, anonymous, reviewer(s) for their contribution to the peer review of this work

Reprints and permissions information is available at www.nature.com/reprints.